remote sensing

MDPI

Article

Integration of Satellite Precipitation Data and Deep Learning for Improving Flash Flood Simulation in a Poor-Gauged Mountainous Catchment

Xuan Tang, Zhaorui Yin, Guanghua Qin, Li Guo and Hongxia Li *

State Key Laboratory of Hydraulics and Mountain River Engineering, College of Water Resource and Hydropower, Sichuan University, Chengdu 610065, China; 2019223060031@stu.scu.edu.cn (X.T.); 2020223060024@stu.scu.edu.cn (Z.Y.); qinguanghua@scu.edu.cn (G.Q.); liguo01@scu.edu.cn (L.G.)
* Correspondence: hongxiali@scu.edu.cn

Abstract: Satellite remote sensing precipitation is useful for many hydrological and meteorological applications such as rainfall-runoff forecasting. However, most studies have focused on the use of satellite precipitation on daily, monthly, or larger time scales. This study focused on flash flood simulation using satellite precipitation products (IMERG) on an hourly scale in a poorly gauged mountainous catchment in southwestern China. Deep learning (long short-term memory, LSTM) was used, merging satellite precipitation and gauge observations, and the merged precipitation data were used as inputs for flood simulation based on the HEC-HMS model, compared with the gauged precipitation data and original IMERG data. The results showed that the application of original IMERG data used directly in the HEC-HMS hydrological model had much lower accuracy than that of gauged data and merged data. The simulation using the merged precipitation in HEC-HMS exhibited much better performances than gauged data. The mean NSE improved from 0.84 to 0.87 for calibration and 0.80 to 0.84 for verification, while the lower NSE improved from 0.81 to 0.84 for calibration and 0.73 to 0.86 for verification, which showed that accuracy and robustness were both significantly improved. Results of this study indicate the advances of remote sensing precipitation with deep learning for flash flood forecasting in mountainous regions. It is likely that more significant improvements can be made in flash flood forecasting by employing multi-source remote sensing products and deep learning merging methods considering the impact of complex terrain.

Keywords: IMERG; satellite precipitation; flash flood forecasting; HEC-HMS; deep learning

check for updates

Citation: Tang, X.; Yin, Z.; Qin, G.; Guo, L.; Li, H. Integration of Satellite Precipitation Data and Deep Learning for Improving Flash Flood Simulation in a Poor-Gauged Mountainous Catchment. *Remote Sens.* **2021**, *13*, 5083. https://doi.org/10.3390/rs13245083

Academic Editor: Qiuhong Tang

Received: 10 November 2021
Accepted: 12 December 2021
Published: 14 December 2021

1. Introduction

Flash flood is one of the most serious natural disasters around the world. The losses from flash floods generally account for about 70% of all flood disasters in China, and the frequency and severity of flash flood disasters are expected to increase with global climate change [1–3].

Flood forecasting is very important for reducing the risk of flash floods [4,5]. Many studies indicated that precipitation data were one of the essential inputs for hydrological modeling, and about 70–80% of the uncertainties of hydrological simulations were due to the uncertainties in precipitation data [2,6–8]. The commonly used precipitation data are (1) rain gauge data, the advantage of which is providing accurate point precipitation information. However, many small catchments with complex topography are poorly gauged, so their spatial representativeness is deficient, which impacts the accuracy of flash flood forecasting [9–11]. (2) Satellite precipitation products (SPPs)—these satellite remote sensing technologies provide new ways for precipitation monitoring, which has wide spatial coverage making up for the inadequate and uneven distribution of ground precipitation observation, especially for ungauged basins [12–15]. Currently, SPPs have become potential precipitation data sources for hydrometeorological studies [16–20].

However, compared with rain gauge data, SPPs have relatively poor precision. Consequently, many efforts have been made recently to merge SPPs and gauge observations to improve the accuracy and spatial coverage of the precipitation estimates before other applications. Many methods have been proposed, such as the simplest linear merging methods [21], bias correction or residual-based methods [22,23], and optimal interpolation methods [24]. Most of the methods above are limited by many assumptions [21,23]. For example, the linear correction method needs to assume a linear relationship between the input and the corrected output sequence. The kriging correction method assumes that the precipitation series conforms to gaussian normal distribution. In recent years, machine learning methods, such as artificial neural networks (ANNs) and support vector machines (SVMs), have been gradually applied to the study of satellite precipitation error corrections. With strong self-learning ability, it has unique advantages in dealing with spatial heterogeneity and nonlinear relational problems without restrictive assumptions. Zhang et al. [25] proposed a double machine learning approach (random forest in combination with the regression models of machine learning algorithms) to merge multiple satellite-based precipitation products and gauge observations over the Chinese mainland.

Compared with traditional machine learning, deep learning has a much stronger ability to better capture abstract spatial or temporal structures hidden in data [26] and has been used in hydrometeorological research, such as image recognition, speech recognition, natural language processing as well as precipitation forecasting [27,28]. Tao et al. [29] compared retrieving precipitation from satellite images using an earlier generation neural network system and a deep learning model, and the results showed the latter had a much better performance. Wu et al. [30] proposed a deep fusion model (convolutional neural network (CNN) combined with long short-term memory (LSTM)) to merge TRMM 3B42 V7 satellite data, rain gauge data, and thermal infrared images by exploiting their spatial and temporal correlations, and the proposed model outperformed other comparative methods. Although deep learning models have recently been found in successful applications in merging SPPs and gauge observations, most studies have focused on assessing merging satellite precipitation on daily, monthly, or larger time scales [31–34], and rarely for flash flood simulation on an hourly scale. There is still a substantial gap between SPPs and gauge observations at the hourly scale [21,35,36], which may not meet the qualified accuracy standards and application requirements.

In previous studies, the orographic effect on satellite precipitation accuracy has been reported. Studies have shown that the satellite–gauge merging results would be affected by complex terrain conditions [10]. Peng et al. [37] evaluated the precipitation detection ability of multiple satellite products in a typical agriculture area of China, and it indicated that the higher the elevation, the lower the performance ability. Bhuiyan et al. [38] provided a multiple machine learning technique (random forest and neural networks) based on error modeling to improve the transferability of the error model among complex terrains over the Brahmaputra River basin.

The objective of this study was to integrate hourly satellite precipitation data and the deep learning method for improving flash flood simulation in a poor-gauged mountainous catchment in southwestern China. To evaluate the precipitation accuracy over the complex terrain of the study area, we firstly compared the remote sensing precipitation with gauged precipitation, and secondly, remote sensing precipitation and gauge observations were merged by the deep learning method for flash flood simulation, and thirdly, precipitation was further validated by flood simulation accuracy reversely. The rest of the paper is arranged as follows. Materials and methods are detailed in Sections 2 and 3, where the study area, data, models, and evaluation criteria are described. Sections 4 and 5 present the obtained results and discussions. Finally, in Section 6, the main conclusions and suggestions for future studies are provided.

2. Materials

2.1. Study Area

The Shouxi River is a small tributary of the Min River (in Sichuan Province), which is a typical mountainous catchment. The Shouxi catchment covers an area of 632 km^2, and the length of the main channel is 56 km. It lies between 102°02′–103°30′ E longitude and 30°50′–31°03′ N latitude and is dominated by a humid subtropical climate (Figure 1). The annual precipitation is 1200–1900 mm, and the annual temperature is 10–20 °C. Landcover is dominated by shrubs. The average elevation is 2174.8 m, and the average river slop is 31.4° (Table 1).

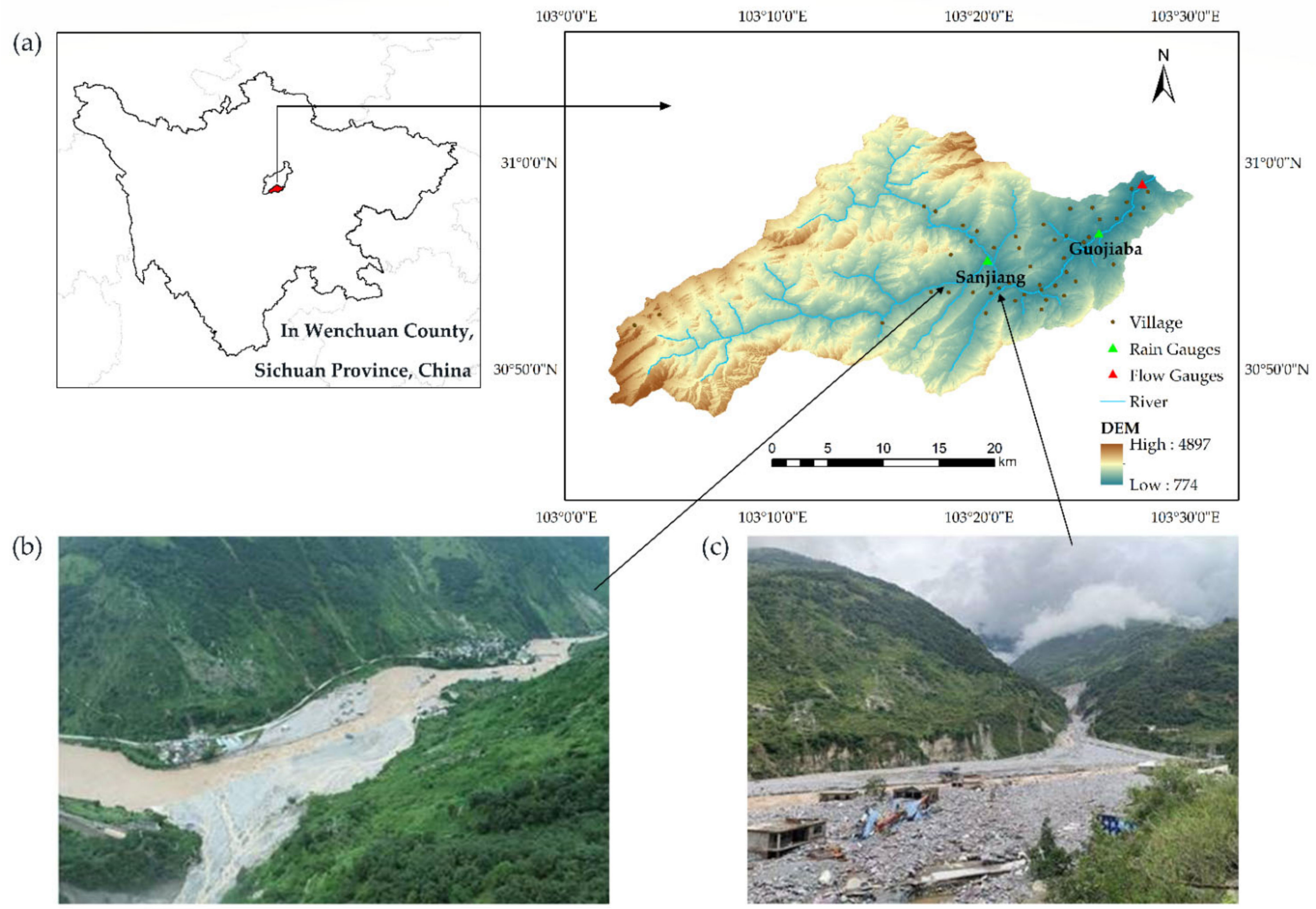

Figure 1. (**a**) Location of Shouxi catchment; (**b**) the top view of disaster site; (**c**) the destroyed village after the flash flood event in August 2020.

Table 1. Physiographic parameters (catchment area, elevation, and river slope).

Area (km^2)	Elevation (m)			River Slope (°)		
	Maximum	Minimum	Average	Maximum	Minimum	Average
600.4	4897.0	774.0	2174.8	87.2	0	31.4

The Shouxi River is located in Wenchuan County, where the 8.2 magnitude earthquake occurred in 2008. Due to the severe earthquake, secondary disasters are more likely to occur after rainstorms and flash floods, which may cause more serious threats to the local economy, social stability, and native lives. Flash floods happen quite frequently in the Shouxi River, and more than five major flash floods have happened in the past 10 years. For example, the heavy storm event that occurred on 20 August 2019 caused a severe flash flood. The storm lasted for 13 h, and the peak flow reached 1860 m^3/s, resulting in losses of lives of close to 50, land damage of more than 300 mu, road damage of 5 km, and economic losses of nearly 200 million RMB. In August 2020, another major flash flood took place in this catchment that caused economic losses of nearly 100 million RMB yuan. The extreme rainfall amounts and the severity of the flood response have made this catchment as a case study for several investigations on flash flood prevention [39–41].

2.2. Data Set

There are two rain gauges (Sanjiang station and Guojiaba station) and one flow gauge (Guojiaba station) in the Shouxi catchment. The location of the rain and flow gauges are shown in Figure 1a.

2.2.1. Hydrometeorological Database

Hourly precipitation and discharge gauge data during 2014–2020 were collected from local meteorological agencies (Table 2).

The IMERG version 6 GPM-Level 3 Final Run product was employed in the study. IMERG data are available in https://disc.gsfc.nasa.gov/ (accessed on 23 August 2020), the website of the NASA Goddard Earth Sciences (GES) Data and Information Services Center (DISC). In the study, we employed the product from 2014 to 2020 with a temporal resolution of 0.5 h, a spatial resolution of $0.1° \times 0.1°$ (Table 2). To maintain consistency between the IMERG and gauged observations, the IMERG-Final adopting coordinated universal time (UTM) was shifted to China Standard Time (CST, UTM + 8 h) [42]. For evaluating and simulating, 0.5 h IMERG-Final was aggregated to 1-h accumulations.

Table 2. Datatype, description, and sources used in this study.

Data Type	Temporal Resolution	Spatial Resolution	Source	Reference
Precipitation gauge data	1 h (2014–2020)	-	Local meteorological agencies	
Discharge data	1 h (2014–2020)	-	Local meteorological agencies	
IMERG-Final data	0.5 h (2014–2020)	$0.1 \times 0.1°$	https://disc.gsfc.nasa.gov/ (accessed on 23 August 2020)	[43]
DEM	-	30×30 m	http://www.gscloud.cn (accessed on 5 July 2020)	
Landuse	-	1×1 km	https://www.resdc.cn/DOI/ (accessed on 5 July 2020)	
Soil	-	1×1 km	FAO, HWSD	[44]

2.2.2. Physiographic Databases

A 30×30 m digital elevation model (DEM) was obtained from the Geospatial Data Cloud in http://www.gscloud.cn (accessed on 5 July 2020), which was used to extract HEC-HMS physiographic parameters such as catchment area, elevation, and river slope (Table 1), and perform terrain processing.

Land use data were collected from the Resource and Environment Science and Data Center (https://www.resdc.cn/DOI/ (accessed on 5 July 2020)) with a resolution of 1 km. The sources of soil data were from FAO, Harmonized World Soil Database (HWSD). After processing in ArcGIS (extract and reclassify), there were five types of soil (Figure 2a), i.e., calcaric cambisols (CMs), eutric regosols (RGe), mollic leptosols (LPm), eutric leptosols (LPe), dystric cambisols (CMd), and haplic luvisols (LVh). Land use data (Figure 2b) were reclassified as agricultural land, mountainous forest, shrub and grassland, architectural land, open space, river, and water.

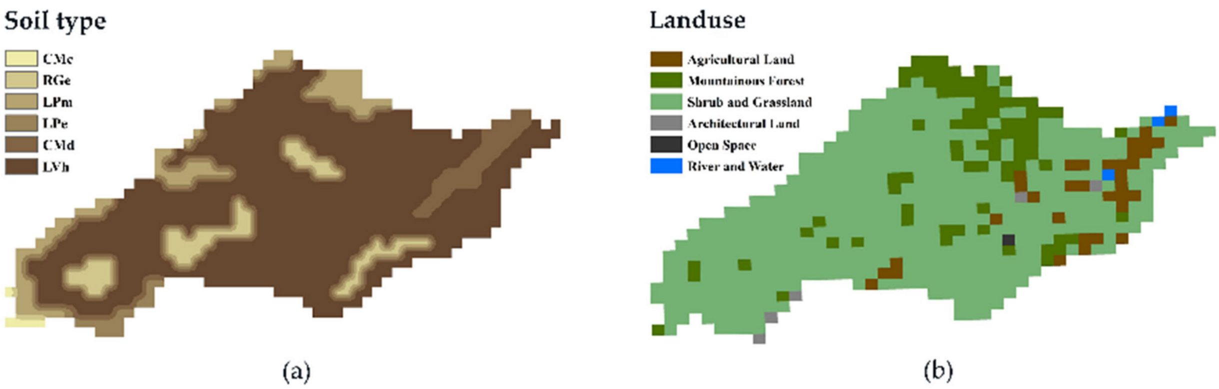

Figure 2. (**a**) Soil types and (**b**) landuse in the Shouxi catchment.

3. Methodology

In this study, three precipitation input schemes were designed based on satellite precipitation data and deep learning for solving ungauged precipitation data in the upper reaches of the Shouxi catchment: scheme 1—inputting the gauged precipitation data (Gauge) as the benchmark for comparison; scheme 2—inputting the original IMERG data (IMERG-original); scheme 3—inputting Gauge merged with IMERG data (Gauge-IMERG) (in Section 3.1) into the model for flood simulation improvement.

3.1. LSTM-Based Satellite-Gauge Merging Method

LSTM network is one of the deep learning techniques that shows a great ability for learning from sequential data by considering information selections and long-term dependencies. LSTM can capture highly complex data distributions through memory units, which are composed of a forget gate, an input gate, and an output gate. The addition of the memory unit in the hidden layer enables the LSTM to learn the state characteristics of the long-period sequence data, making the memory information in the time series controllable, thereby solving the notorious problem of the exploding or vanishing recurrent neural network (RNN) gradient.

Figure 3 presents the framework of the LSTM-based methods used to merge SPPs and gauge observations. The observed satellite data of the 5th and 6th grid (corresponding to gauge observations downstream of the catchment) at time *t* and the 4th and 9th grid (represent upstream precipitation) at time $(t - 1)$ were normalized by the max–min method and input into LSTM (Figure 3). Then, the forward propagation equations of the present LSTM-based model could be summarized as the following:

$$f_t = \sigma\left(U_f x_t + W_f h_{t-1} + b_f\right) \tag{1}$$

$$\sigma(x) = \frac{1}{1 + e^{-x}} \tag{2}$$

$$i_t = \sigma(U_i x_t + W_i h_{t-1} + b_i) \tag{3}$$

$$\bar{c}_t = \tanh(U_{\bar{c}} x_t + W_{\bar{c}} h_{t-1} + b_{\bar{c}}) \tag{4}$$

$$\tanh(x) = \frac{e^x - e^{-x}}{e^x + e^{-x}} \tag{5}$$

$$c_t = f_t \odot c_{t-1} + i_t \odot \tilde{c}_t \tag{6}$$

$$o_t = \sigma(U_o x_t + W_o h_{t-1} + b_o) \tag{7}$$

$$h_t = o_t \odot \tanh(c_t) \tag{8}$$

$$y_t = W_d h_t + b_d \tag{9}$$

where f_t, i_t, and o_t are, respectively, the forget, input, and output gates; σ is the sigmoid activation function; U is the rectified linear unit; Ws are network weights; bs are bias parameters; c_t represents the states of memory cells; $\odot$ denotes pointwise multiplication; h_t represents hidden states; y_t is the predicted output, which is compared to satellite observations.

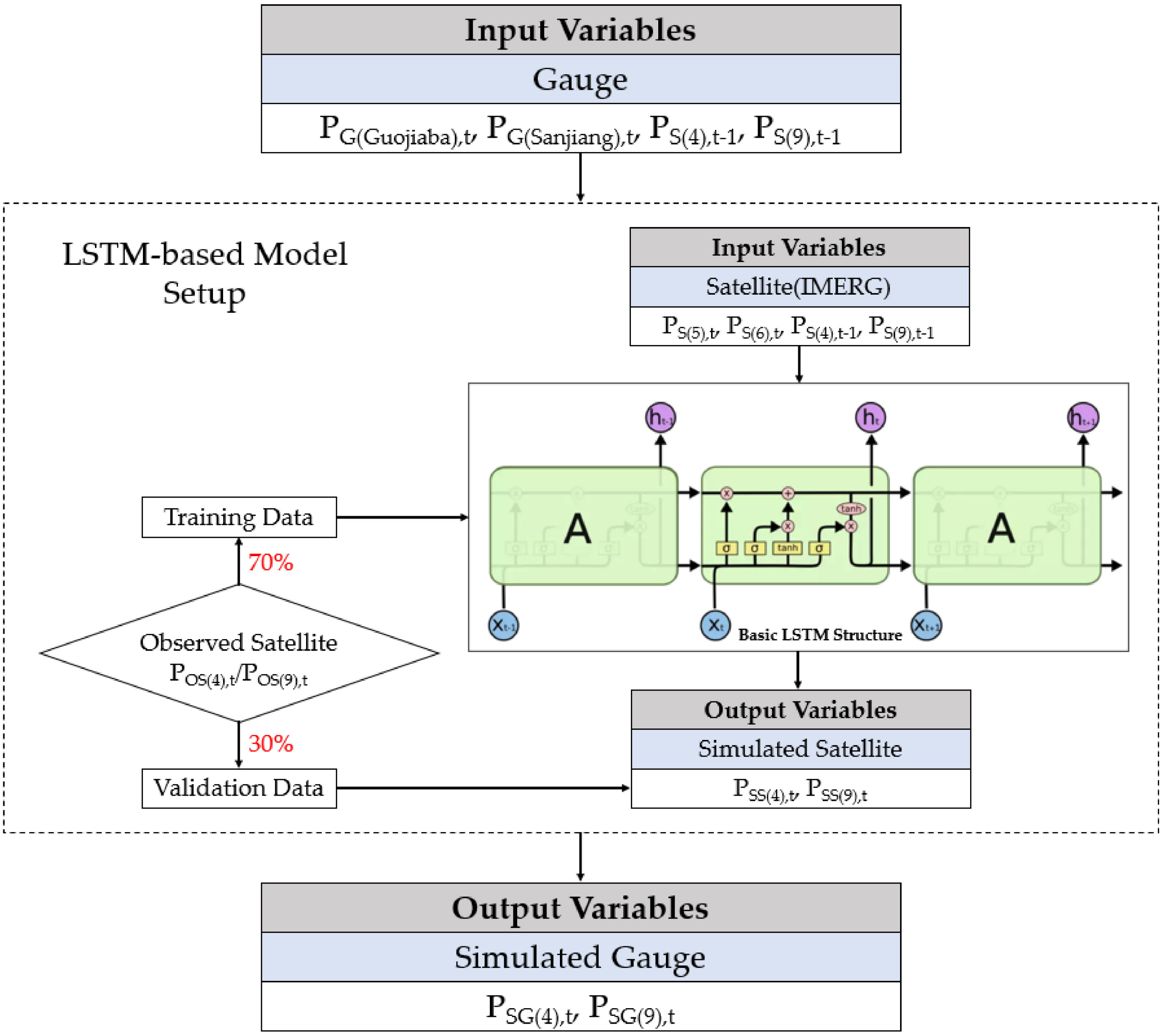

Figure 3. Framework of the LSTM−based methods used to merge SPPs and gauge observations: $P_{G(i),t}$ is gauge precipitation; $P_{S(i),t}$ is satellite precipitation; $P_{SG(i),t}$ is simulated gauge precipitation; $P_{SS(i),t}$ is simulated satellite precipitation; i is the location of observation; for gauge observations, i represents Guojiaba/Sanjiang; for satellite observations, i represents the grid number marked in Figure 4.

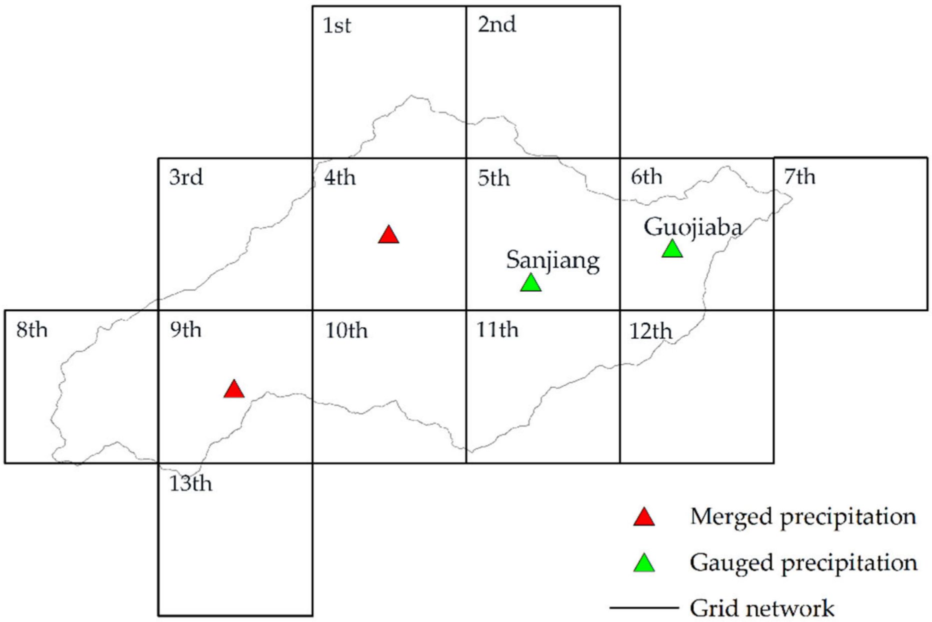

Figure 4. Distribution of grid networks and gauged/merged precipitation.

(1) Parameter Setting

Hidden layer number, neuron number, and training times are the main impact factors of the LSTM training. Although increasing the number of hidden layers of the neural network can improve convergence accuracy, Villiers and Barnard [45] showed that the neural network consisting of two hidden layers had poor robustness and low convergence accuracy. Hornik et al. [46] proved that a single hidden layer neural network with enough neurons could complete any measurable functional relationship from input data to output data and achieve the desired accuracy. Therefore, the initial settings of LSTM in the research were as follows: the hidden layer is 1 layer, the hidden layer contains 10 neurons, the learning rate is 0.0005, and the number of training times is 10. The simulated satellite precipitation process would be adjusted by changing the number of neurons in the hidden layer (10, 20, 30, 40, 60, 80, 100, 120, and 150) and training times (10, 20, 30, 40, 50, 100, 150, 200, and 300).

(2) Training and Validation

In the study, the gauge observations were subdivided into two parts (i.e., 70% and 30%); one was used as the training dataset, while the other was the validation dataset. R^2 was used to evaluate the predicted results. When the number of neurons was 100 and the number of training times was 200, the R^2 of training (calibration) and verification reached 0.89 and 0.81 (Figure 5), which showed the best relationship between the observed satellite data and the simulated satellite data at 4th and 9th grid.

(3) Output Merged Data

Finally, Gauge observed data of Guojiaba and Sanjiang station at time t and the 4th and 9th grid at time ($t - 1$) were input into the adjusted LSTM-based model, thus generating merged data at the 4th and 9th grid.

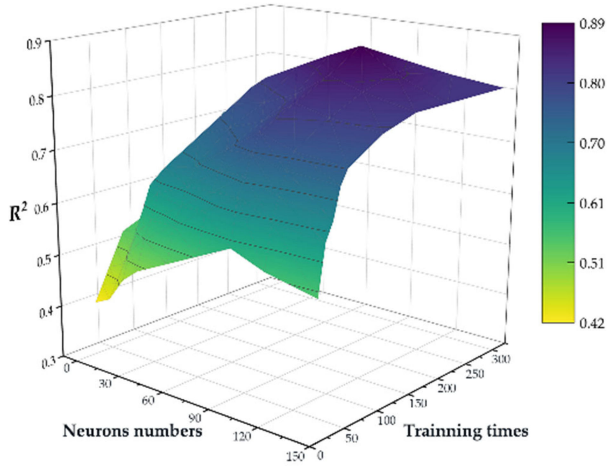

Figure 5. Effects of neuron numbers and training times adjustment on simulation results.

3.2. Hydrological Model

In this study, a physically based semi-distributed Hydrologic Engineering Center's Hydrologic Modelling System (HEC-HMS) was used. It was designed by the US Army Corps of Engineers in 1998 and has been applied for flood simulations in a multitude of scientific applications [47,48]. The main idea of HEC-HMS modeling is to, firstly, build a digital river watershed relying on HEC-GeoHMS, and then import the digital river watershed into the model. By setting and debugging four model components (basin models, meteorological model, control specifications, and time series data), the calculation of rainfall-runoff simulation can be completed.

3.2.1. Preprocessing

The HEC-GeoHMS is designed to process geospatial data and create input files for the HEC-HMS model under a GIS environment [49,50]. In this study, the HEC-GeoHMS was used to calculate DEM data, delineate sub-basins, and construct the river network of the catchment. All hydrological elements were connected to the network in order to model the relationship between precipitation and flow. Figure 6 shows that the Shouxi catchment was divided into 11 sub-basins, depending on the characteristics of land use, soil, and the DEM.

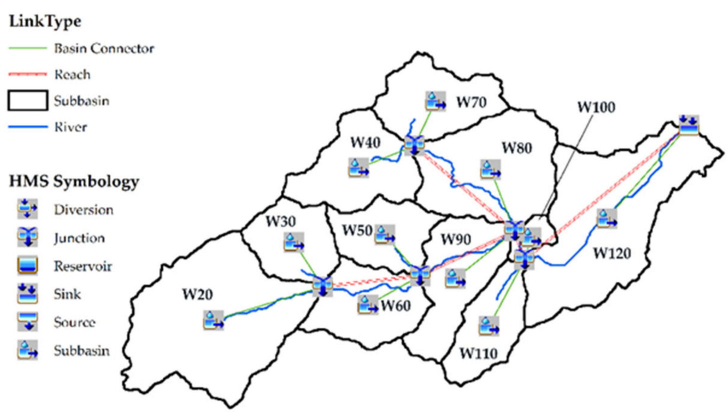

Figure 6. Catchment subdivision of Shouxi catchment.

3.2.2. Model Setup

The HEC-HMS model has four model components: basin model, meteorological model, control specifications, and time series data.

(1) Basin Model

The basin model has a set of hydrological modeling options, i.e., seven types of precipitation loss, seven types of direct runoff (transform), five types of baseflow methods, and eight types of routing methods [51,52]. Based on the characteristics of the Shouxi catchment, we used methods of the SCS curve number, SCS unit hydrograph, recession, and Muskingum to simulate the flood discharge. Figure 7 presents the main parameters of the basin model. The curve number (*CN*) is a physical parameter determined by soil types, land uses, and the antecedent moisture condition (AMC) of each sub-basin, etc. [51]. It was calculated for each sub-basin by the Generate *CN* Grid tool of the HEC-GeoHMS. The lag time (t_{lag}) depended on *CN* and used the *CN* lag method to estimate. The initial discharge of baseflow (Q_0) and the recession index (k) were based on the process of observed runoff. The travel time K was calculated by the TR-55 method, and the degree of storage (x) was assumed 0.47 by trial and error [47].

(2) Meteorological Model

The meteorological model holds information related to precipitation data. In this paper, three kinds of precipitation data, Gauge, IMERG-original, and Gauge-IMERG, were used as input for the HEC-HMS model to simulate the flash flood at the Shouxi catchment.

(3) Control Specifications

Control specifications are used to set the timing of the simulation to use in the model, such as the initial time and terminal time of a storm, what type of time interval (second, minute, hour, or day). In this study, we used hourly time steps for flash flood simulating.

(4) Time Series Data

Finally, the time series data component contains parameters or boundary conditions for basin and meteorological models. The main time series data used for this study were three kinds of precipitation data, observed stream flow, and different basin characteristics resulting from the HEC-GeoHMS process.

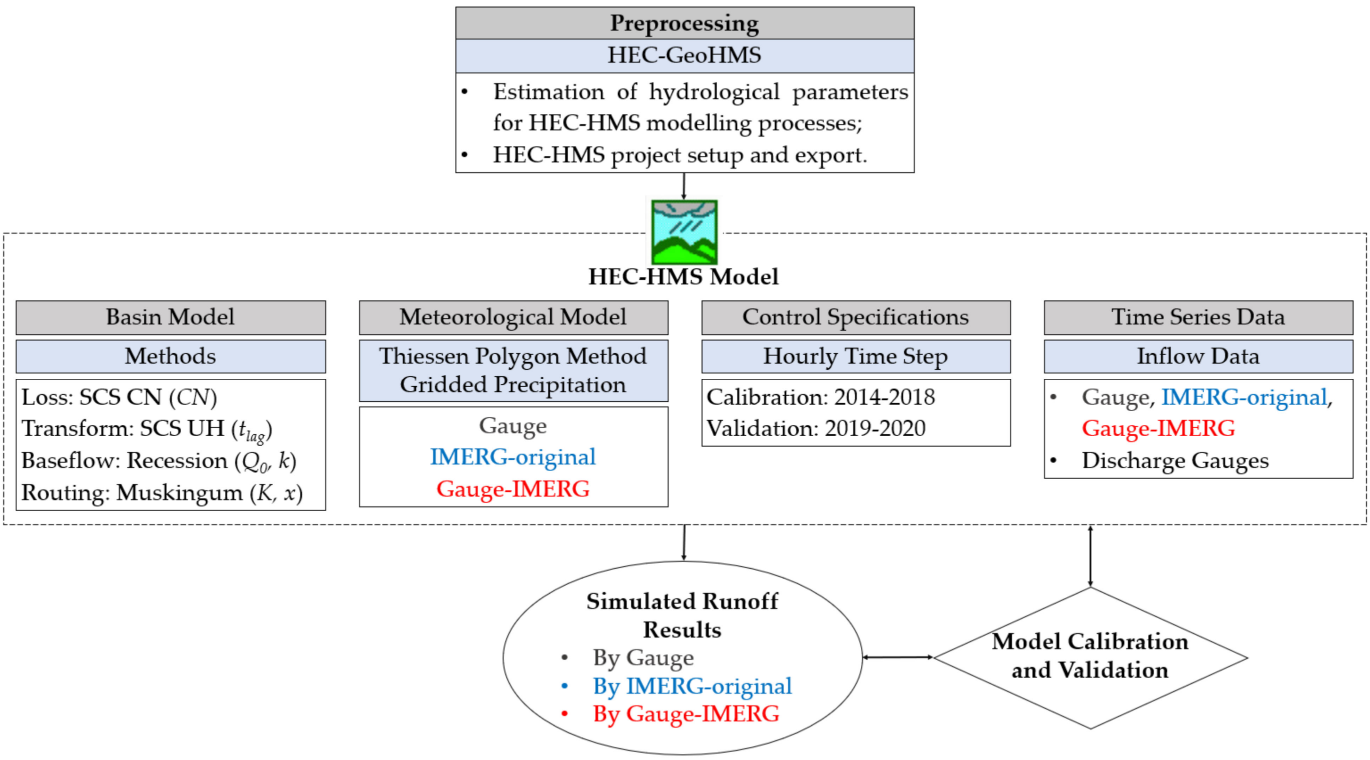

Figure 7. Methodology used for HEC-HMS model for the research.

3.2.3. Model Calibration and Validation

The model was calibrated by observed stream flow. Optimization trials were implemented to calibrate the parameters so as to improve the calibration results the HEC-HMS model can achieve in terms of either manual or automated calibration (such as univariate gradient optimization) [53]. We used a combination of the two calibration methods. In this study, the curve number (CN) in the SCS curve number method and the lag time (t_{lag}) in the SCS unit hydrograph were adjusted to the best possible match for the observed stream flow in terms of peak value/time and shape of the hydrograph. The model calibration was performed with the objective function of the peak-weighted root mean square error (PWRMS).

For validation, it is the process of testing model capability to simulate observed data with acceptable accuracy. Throughout this process, calibrated model parameters must be kept constant. In this study, the model was calibrated for 6 years (2014–2018) and 2019–2020 for validation.

3.2.4. Model Evaluation

The observed hourly precipitation and discharge data from 2014 to 2020 were used for simulation. A total of 20 flash flood events in 2014–2020 were chosen for calibrating and validating the HEC-HMS model, with data from 2014–2018 for calibration and 2019–2020 for validation.

Nash–Sutcliffe efficiency (NSE), relative bias (BIAS), and root mean square error (RMSE) were used to evaluate rainfall–runoff simulation process results. The error of peak discharge (EPD) was used to assume the ability of the model to simulate peak discharge, and the max of all peak discharge in an event was used as an indicator. The ideal values for NSE, BIAS, RMSE, and EPD are 1, 0, 0, 0, respectively. All functions are as follow:

$$\text{NSE} = 1 - \frac{\sum_{i=1}^{n} (Q_{S,i} - Q_{G,i})^2}{\sum_{i=1}^{n} (Q_{G,i} - \overline{Q}_G)^2} \tag{10}$$

$$\text{BIAS} = \frac{\sum_{i=1}^{n} (Q_{S,i} - Q_{G,i})}{n} \tag{11}$$

$$\text{RMSE} = \sqrt{\frac{\sum_{i=1}^{n} (Q_{S,i} - Q_{G,i})^2}{n}} \tag{12}$$

$$\text{EPD} = \frac{Q_{S,t} - Q_{G,t}}{Q_{G,t}} \times 100\% \tag{13}$$

where Q_S is the simulated discharge at time t, Q_G is the gauged discharge at time t, and n is time steps in a given event.

4. Results

4.1. Accuracy Evaluation of Satellite Precipitation

The accuracy of satellite precipitation is evaluated. Figure 8 shows the scatter plots of IMERG versus the gauged precipitation at Guajiaba and Sanjiang stations. IMERG at Guojiaba and Sanjiang stations both show large spread at an hourly resolution with R^2 = 0.14 and 0.12. In Table 3, the correlation coefficient (CC) is unsatisfactory, with 0.36 and 0.51 at two grids. The IMERG data show overestimation according to RMSE and BIAS (Table 3).

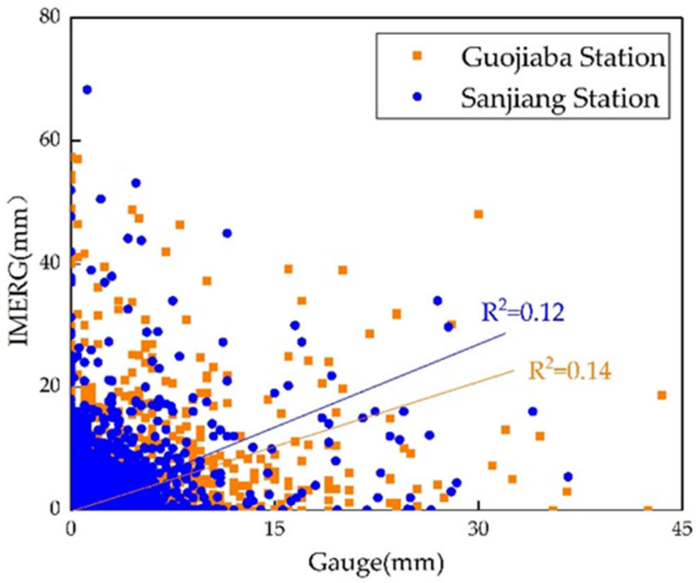

Figure 8. Scatterplots of ground-observed precipitation versus satellite-observed precipitation from IMERG products at Guojiaba station and Sanjiang station.

Table 3. Summary of accuracy evaluation of IMERG products at Guojiaba station and Sanjiang station.

Station	Evaluation Criteria		
	CC	**RMSE**	**BIAS**
Guojiaba	0.36	1.45	0.09
Sanjiang	0.51	1.58	0.1

4.2. Overall Performance of Different Precipitation Data for Flood Simulation

The model driven by gauged precipitation is used as the benchmark for comparison. The results show that the mean NSE using gauged precipitation data is 0.84 for calibration and 0.80 for validation (Figure 9 and Table 4), which has an acceptable capability to simulate flood discharge. However, the simulated discharge in some events is in poor agreement with the observed duo to ungauged data upstream of the catchment (as discussed in Section 5.1); for example, the event in 24 July 2016 (NSE = 0.7) and 16 August 2020 (NSE = 0.64) shown in Table 5.

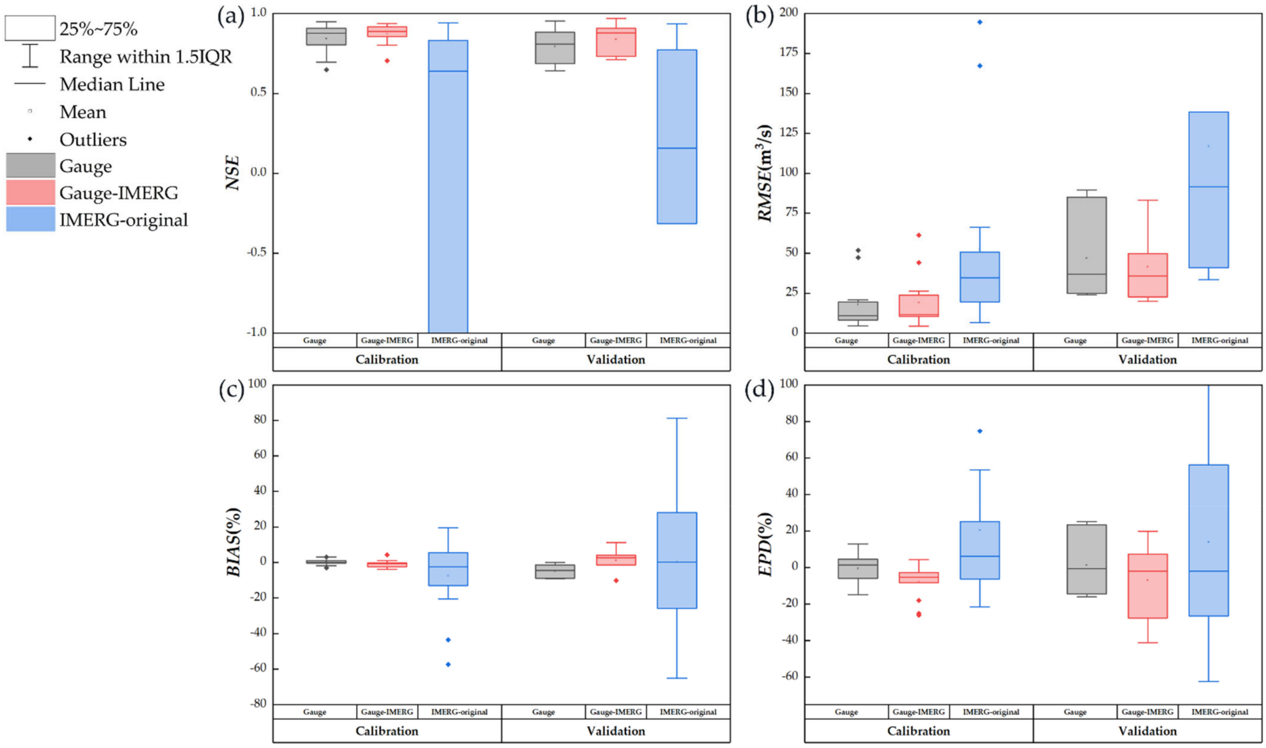

Figure 9. Statistical indices of three precipitation inputs (Gauge, IMERG−original, and Gauge−IMERG): (**a**) *NSE;* (**b**) *RMSE*; (**c**) *BIAS*; (**d**) *EPD* for calibration (C) and validation (V).

Table 4. Evaluation criteria for 20-event flood simulations.

Statistical Indicators		Gauge		IMERG-Original		Gauge-IMERG	
		Calibration	Validation	Calibration	Validation	Calibration	Validation
NSE	Mean	0.84	0.80	−1.22	−1.33	0.87	0.84
	Lower quartile	0.81	0.72	−2.31	−0.13	0.86	0.75
	Median	0.88	0.81	0.64	0.16	0.89	0.88
	Upper quartile	0.91	0.86	0.83	0.57	0.92	0.90
	Range	[0.65, 0.95]	[0.64, 0.95]	[−9.72, 0.94]	[−11.26, 0.94]	[0.7, 0.94]	[0.71, 0.97]
RMSE (m^3/s)	Mean	17.84	46.83	52.40	116.95	19.04	41.67
	Lower quartile	8.14	25.28	19.58	50.39	10.47	27.92
	Median	11.01	36.87	34.59	91.48	11.51	35.68
	Upper quartile	19.51	63.34	50.71	134.83	23.74	48.59
	Range	[4.54, 51.75]	[24.07, 89.64]	[6.68, 194.71]	[33.39, 323.31]	[4.26, 61.37]	[19.85, 83.14]
BIAS (%)	Mean	0.2%	−4.8%	−7.6%	0.5%	−0.9%	1.3%
	Lower quartile	−0.5%	−7.8%	−13.1%	−20.9%	−2.5%	−0.7%
	Median	−0.1%	−4.5%	−2.5%	0.2%	−0.7%	2.5%
	Upper quartile	0.9%	−2.0%	5.5%	14.5%	−0.2%	3.4%
	Range	[−3.0%, 3.1%]	[−9.3%, −0.1%]	[−57.4%, 19.5%]	[−65.2%, 81.2%]	[−3.8%, 4.3%]	[−10.2%, 11.1%]
EPD (%)	Mean	−0.6%	1.4%	20.5%	14.0%	−7.8%	−6.9%
	Lower quartile	−5.9%	−13.5%	−6.3%	−17.2%	−8.3%	−15.8%
	Median	1.4%	−0.6%	6.0%	−2.0%	−5.3%	−1.9%
	Upper quartile	4.6%	14.2%	25.2%	42.1%	−2.7%	3.4%
	Range	[−14.9%, 12.8%]	[−16.0%, 25.5%]	[−21.5%, 117.7%]	[−62.3%, 112.3%]	[−26.0%, 4.4%]	[−41.1%, 19.8%]

Table 5. Results of 20-event flood simulations in the Shouxi catchment.

Events	NSE			RMSE (m^3/s)			BIAS (%)			EPD (%)		
	Gauge	IMERG-Original	Gauge-IMERG	Gauge	IMERG-Original	Gauge-IMERG	Gauge	IMERG-Original	Gauge-IMERG	Gauge	IMERG-Original	Gauge-IMERG
12 September 2014	0.81	0.46	0.80	10.62	19.58	11.51	−1.5%	19.2%	−3.8%	3.6%	−21.5%	0.3%
22 September 2015	0.77	0.75	0.90	6.50	6.68	4.26	0.8%	−2.5%	−0.5%	1.4%	3.5%	−3.8%
14 July 2016	0.93	0.94	0.94	11.01	10.05	10.47	0.2%	5.5%	−3.8%	4.6%	−8.0%	1.8%
24 July 2016	0.70	−5.92	0.92	8.14	40.65	4.49	3.1%	−0.5%	4.3%	1.8%	74.7%	−5.3%
26 July 2016	0.88	−9.72	0.80	20.85	194.71	26.33	−3.0%	−57.4%	1.0%	−14.9%	117.7%	−25.1%
4 August 2017	0.95	0.51	0.93	7.85	35.31	13.83	3.0%	−20.6%	0.9%	−1.7%	14.5%	−8.3%
25 August 2017	0.91	0.75	0.88	19.51	34.59	23.74	2.1%	8.2%	−1.3%	11.2%	22.2%	−17.9%
28 August 2017	0.89	0.83	0.86	47.23	66.20	61.37	0.9%	−12.2%	−0.7%	−14.7%	1.5%	−26.0%
9 July 2018	0.84	0.64	0.92	15.54	22.68	10.70	−0.5%	−13.1%	−0.4%	6.4%	25.2%	4.4%
10 July 2018	0.89	−2.31	0.88	4.54	24.48	4.64	−0.1%	19.5%	−0.2%	−0.4%	−17.0%	−2.7%
11 July 2018	0.93	−4.50	0.91	19.01	167.38	21.05	−0.1%	−43.5%	−3.5%	−5.9%	53.4%	−7.8%
19 July 2018	0.65	0.84	0.70	9.45	8.18	10.90	−1.9%	−2.8%	−2.5%	12.8%	6.0%	−3.6%
20 July 2018	0.82	0.85	0.89	51.75	50.71	44.16	−0.1%	1.5%	−1.0%	−11.9%	−6.3%	−7.8%
21 August 2019	0.81	0.16	0.88	41.58	91.48	35.68	−6.8%	−15.9%	2.5%	−14.5%	56.2%	−1.9%
22 August 2019	0.88	0.36	0.91	24.07	59.82	22.71	−0.1%	28.1%	2.7%	−0.6%	−26.5%	7.4%
26 June 2020	0.95	−0.32	0.97	24.84	131.28	19.85	−1.5%	81.2%	0.1%	−12.6%	−62.3%	−4.0%
7 August 2020	0.76	−11.26	0.71	36.87	323.31	49.68	−8.9%	−65.2%	11.1%	−16.0%	112.3%	−41.1%
12 August 2020	0.84	0.77	0.78	25.71	33.39	33.12	−2.5%	0.2%	4.1%	4.9%	−2.0%	−27.7%
16 August 2020	0.64	0.05	0.89	85.09	138.37	47.50	−9.3%	−25.9%	−1.4%	25.0%	27.9%	−0.6%
31 August 2020	0.69	0.94	0.73	89.64	40.96	83.14	−4.5%	0.9%	−10.2%	23.4%	−7.8%	19.8%

The results show that the IMERG-original has worse performance in predicting the flood. It is observed that the LSTM model is unable to capture the flash flood, as a negative NSE value is predicted. The mean NSE is −1.22 for calibration and −1.33 for validation (Figure 9 and Table 4). Results indicate that precipitation errors are further propagated to rainfall–runoff simulations, leading to much lower accuracy than using gauged precipitation to forecast (Figure 9 and Table 4).

The results of using Gauge-IMERG data exhibit much better performances. The mean NSE improves from 0.84 to 0.87 for calibration and 0.80 to 0.84 for verification, while the lower NSE from 0.81 to 0.84 for calibration and 0.73 to 0.86 for verification (Figure 9 and Table 4). The same results are also observed in RMSE, BIAS, and EPD (Figure 9), which illustrate that the accuracy and robustness are both significantly improved.

4.3. Performance Assessment of Typical Flood Events Simulation

We choose the events of 24 July 2016 and 16 August 2020 as two typical flood events. The event of 24 July 2016 represents the most common single-peak flood process, and the event of 16 August 2020 represents multi-peak and major floods. Figure 10 is the simulation results of two typical flood events using three precipitation datasets. We can see that, in the flood event 24 July 2016, the simulation of Gauge-IMERG outperforms that of the other two, with the NSE rising from 0.7/−5.92 for the other two to 0.92 (Table 6). The errors of time to the peak discharge simulation using merged data are 0 h, which also show a better performance than that of using the other two data. The simulation of peak discharge (EPD) using merged precipitation is much better than that using original data (74.7% and −5.3%, respectively). A similar improvement can also be observed in the event of 16 August 2020. The NSE is improved from 0.64/0.05 for the other two to 0.89 (Table 6). The RMSE from the merged precipitation is 37.59 m^3/s and 90.87 m^3/s less than that from the original data and gauged data, respectively. The simulation of peak discharge (EPD) using merged precipitation is improved from 25.0%/27.9% to −0.6%. The results exhibit that the LSTM-based merging method has a better performance for flash flood simulation.

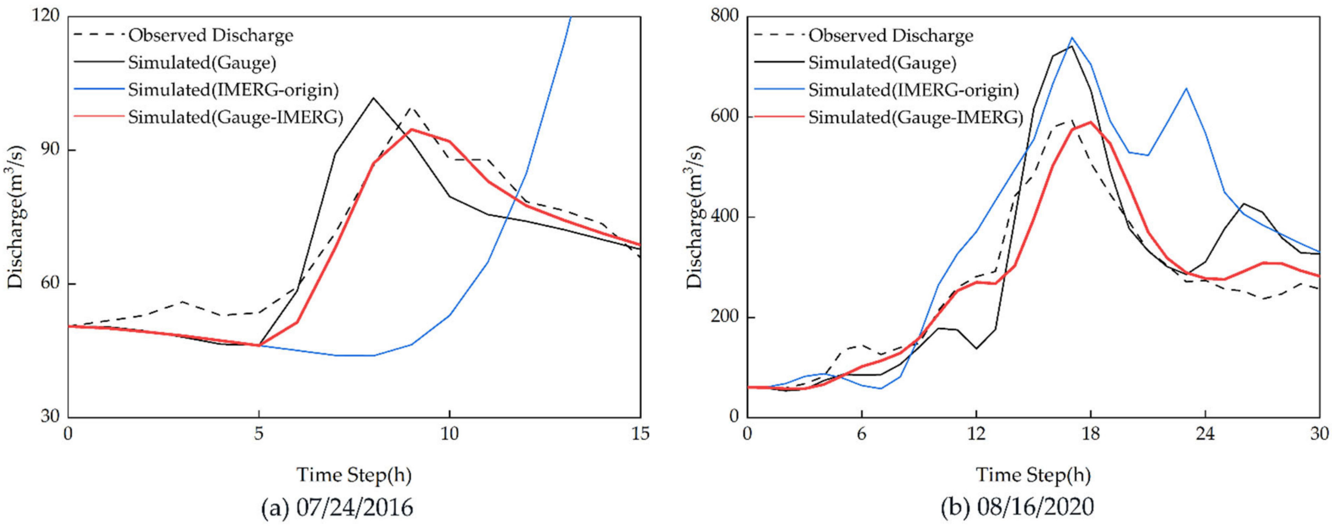

Figure 10. Flood discharge simulation by using four precipitation datasets for two typical events (the events of 24 July 2016 (**a**) in calibration and 16 August 2020 (**b**) in validation).

Table 6. Statistical indices of the event in 24 July 2016 (the actual peak discharge = 100 m^3/s, time to peak = 9 h) and 16 August 2020 (the actual peak discharge = 593 m^3/s, time to peak = 17 h).

Events	Precipitation Inputs	Error of Time to Peak (h)	Peak Disch (m^3/s)	NSE	RMSE (m^3/s)	BIAS	EPD
24 July 2016	Gauge	1	101.8	0.70	8.14	3.1%	1.8%
	IMERG-origin	6	174.7	−5.92	40.65	−0.5%	74.7%
	Gauge-IMERG	0	94.7	0.92	4.49	4.3%	−5.3%
16 August 2020	Gauge	0	741.3	0.64	85.09	−9.3%	25.0%
	IMERG-origin	0	758.7	0.05	138.37	−25.9%	27.9%
	Gauge-IMERG	1	589.7	0.89	47.50	−1.4%	−0.6%

5. Discussion

5.1. Validating the LSTM-Based Satellite-Gauge Merging Method

The Gauge-IMERG input in HEC-HMS shows much better performances because it improves the spatial distribution, which was made despite the lack of precipitation data upstream of the Shouxi catchment. Figure 11 shows the differences in the spatial precipitation distribution between gauged precipitation (a)/merged precipitation (b) in the event of 16 August 2020. The areal precipitation of upstream based on gauged data was calculated by the Thiessen Polygon, the same as the gauged precipitation at Sanjiang station (136 mm), due to lack of observation in the upper reaches of the Shouxi catchment. However, a significant difference in the distribution of precipitation is shown when using the merged data. The precipitation upstream is much lower than downstream in the event of 16 August 2020; that is, the precipitation is 84.4 mm upstream, 50 mm less than Gauge (136 mm) (Table 7).

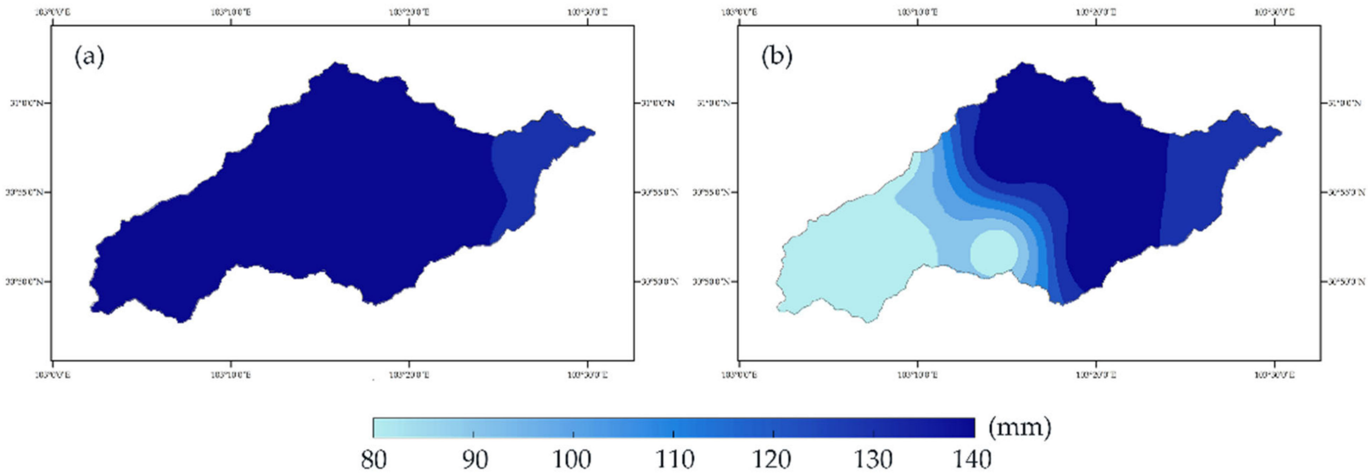

Figure 11. The spatial precipitation distribution of gauged precipitation (**a**) /merged precipitation (**b**) in the event of 16 August 2020.

Table 7. Comparison between Gauge and Gauge-IMERG on the precipitation amount and peak discharge/time in the event of 16 August 2020.

Type of Inputs	**Precipitation Amount (mm)**		**Discharge**			
			Peak Discharge (m^3/s)		**Peak Time (h)**	
	Upstream	**Downstream**	**Upstream**	**Downstream**	**Upstream**	**Downstream**
Gauge	136	128	361.3	184.7	16	16
Gauge-IMERG	84.4	131.9	189.8	205.1	18	17

The difference in precipitation leads to a difference in flood simulation. The spatial distribution information of precipitation has a very important impact on the formation of runoff in a physical sense, especially the formation of peak discharge [54,55]. HEC-HMS, as a semi-distributed hydrological model, is driven by distributed precipitation and so it can simulate the runoff of each sub-catchment. Figure 12a,b is the flood simulation of sub-catchment W20 located upstream and W120 downstream. For W20, the results show a great distinction between the discharge process simulated by the two schemes, especially in peak discharge (Figure 12a), because of the differences in precipitation upstream (as shown in Figure 11). The peak discharge of Gauge is 361.3 m^3/s, which is much larger than that of Gauge-IMERG (189.8 m^3/s), while the peak time is a 2-h difference. With respect to downstream (W120), the two simulated flow processes are quite similar, and the peak discharge is 128 and 131.9 m^3/s, respectively (Table 7). The peak time of Gauge-IMERG, affected by the upstream, is 1 h behind Gauge. These observations are why the results in Figure 10b show that the simulated discharge is overestimated by using the Gauge data and improved by using the merged data.

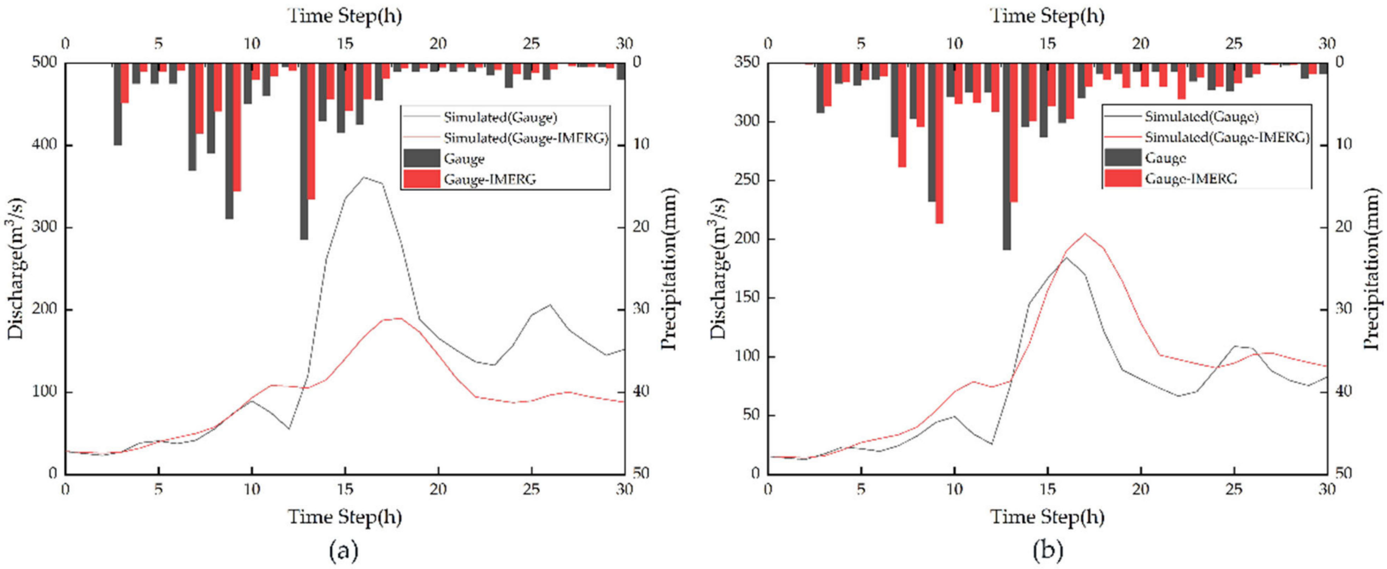

Figure 12. Simulated hydrographs of sub-catchment W20 (**a**) and W120 (**b**) in the event of 16 August 2020, respectively.

5.2. Uncertainties of Satellite Precipitation Products (SPPs) over Complex Terrains

Precipitation gauges are usually sparse in many catchments and generally situated in lowlands under accessibility considerations, especially in regions with complex terrains; thus, underrepresenting precipitation may occur in highlands [32]. SPPs offer a potentially viable solution to observation coverage problems and hydrometeorological application in complex terrain areas. However, the uncertainty of SPPs would be increased over the regions with complex topography, and precipitation estimates can be associated with significant error due to variability and uncertainty introduced by orographic effects. In prior studies, Mei et al. [56] investigated the error characteristics of satellite precipitation products and their error propagation in flow simulations for a range of mountainous basin scales. Results suggested a positive correlation between systematic error and basin elevation. Derin et al. [32] evaluated the performance of four SPPs over a typical complex topography that exerts strong controls on the precipitation regime. Results indicated the evaluated SPPs generally had difficulty in representing the precipitation gradient normal to the orography, and precipitation was underestimated during winter. In addition, complex terrain conditions would affect the satellite–gauge merging results. Zhang et al. [25] proposed a novel double method and applied it over mainland China; the results showed that the proposed method performed better than the other method in most sub-regions except the Tibetan Plateau (QTP), which, with a complex terrain, showed worse performance using the proposed method. In summary, performances of SPPs vary significantly over topographically complex regions and are complicated by significant elevation change. Therefore, the effects of complex terrain on SPP estimates need more consideration.

In this paper, the Shouxi catchment consists of a highly complex terrain with elevation differences greater than 4000 m and slopes ranging from 0° to 60°. Although the integration of satellite precipitation data and deep learning fixes the issues of lack of upstream data and improves the accuracy of flood forecasting to some extent, the impact of complex terrain still needs further investigation of the satellite–gauge merging method in the future. Geographical and topographical covariates, such as elevation, soil type, land type, and soil moisture [38], need to be considered as input variables for merging models based on deep learning.

6. Conclusions

Satellite remote sensing precipitation has a high spatio-temporal resolution but needs to be assessed and corrected/merged before being used in hydrological research. In this study, the performance of the IMERG product for a poor-gauged mountainous catchment in China was assessed, and deep learning was used for precipitation data merging. The merged precipitation data, compared with the gauged data and original IMERG data, were used as inputs for flood simulation based on the HEC-HMS model. The results showed that the HEC-HMS flood discharge simulation using merged precipitation data exhibited much better performances, with NSE greatly improved. The results indicated the good performance of the method proposed in this study and also revealed a high potential for the application of IMERG in other mountainous and data-sparse watersheds in the world. It is suggested that future work should focus on employing multi-source remote sensing products and deep learning merging methods considering the impact of complex terrains to further improve flash flood forecasting.

Author Contributions: Conceptualization, H.L. and X.T.; methodology, H.L. and X.T.; software, X.T. and Z.Y.; validation, X.T.; formal analysis, H.L. and X.T.; investigation, H.L., X.T. and G.Q.; resources, X.T. and Z.Y.; data curation, H.L. and X.T.; writing—original draft preparation, X.T. writing—review and editing, all authors; visualization, H.L. and X.T.; supervision, H.L. and L.G.; project administration, H.L.; funding acquisition, H.L. All authors have read and agreed to the published version of the manuscript.

Funding: This research was funded by the National Key Research and Development Program of China (Grant No. 2019YFC1510700) and the National Natural Science Foundation of China (Grant No. 51979177). Any opinions, findings, and conclusions or recommendations expressed in this material are those of the authors and do not necessarily reflect the views of the funding agencies.

Institutional Review Board Statement: Not applicable.

Informed Consent Statement: Not applicable.

Data Availability Statement: The data and codes used for this study are available from the corresponding author upon request.

Acknowledgments: The authors would like to acknowledge the TRMM and GPM research communities for making the data available to international users and the provider of Gauge observation data.

Conflicts of Interest: The authors declare no conflict of interest.

References

1. Kleinen, T.; Petschel-Held, G. Integrated assessment of changes in flooding probabilities due to climate change. *Clim. Chang.* **2007**, *81*, 283–312. [CrossRef]
2. Todini, E. Flood Forecasting and Decision Making in the new Millennium. Where are We? *Water Resour. Manag.* **2017**, *31*, 3111–3129. [CrossRef]
3. Beniston, M. Trends in joint quantiles of temperature and precipitation in Europe since 1901 and projected for 2100. *Geophys. Res. Lett.* **2009**, *36*. [CrossRef]
4. Borga, M.; Anagnostou, E.N.; Blöschl, G.; Creutin, J.D. Flash flood forecasting, warning and risk management: The HYDRATE project. *Environ. Sci. Policy* **2011**, *14*, 834–844. [CrossRef]
5. Norbiato, D.; Borga, M.; Dinale, R. Flash flood warning in ungauged basins by use of the flash flood guidance and model-based runoff thresholds. *Meteorol. Appl.* **2009**, *16*, 65–75. [CrossRef]
6. Gebregiorgis, A.S.; Hossain, F. Understanding the Dependence of Satellite Rainfall Uncertainty on Topography and Climate for Hydrologic Model Simulation. *IEEE Trans. Geosci. Remote Sens.* **2013**, *51*, 704–718. [CrossRef]
7. Sangati, M.; Borga, M.; Rabuffetti, D.; Bechini, R. Influence of rainfall and soil properties spatial aggregation on extreme flash flood response modelling: An evaluation based on the Sesia river basin, North Western Italy. *Adv. Water Resour.* **2009**, *32*, 1090–1106. [CrossRef]
8. Viglione, A.; Chirico, G.B.; Woods, R.; Blöschl, G. Generalised synthesis of space–time variability in flood response: An analytical framework. *J. Hydrol.* **2010**, *394*, 198–212. [CrossRef]
9. Levizzani, V.; Kidd, C.; Aonashi, K.; Bennartz, R.; Ferraro, R.R.; Huffman, G.J.; Roca, R.; Turk, F.J.; Wang, N.Y. The activities of the international precipitation working group. *Q. J. R. Meteorol. Soc.* **2018**, *144*, 3–15. [CrossRef]

10. Sungmin, O.; Kirstetter, P.E. Evaluation of diurnal variation of GPM IMERG-derived summer precipitation over the contiguous US using MRMS data. *Q. J. R. Meteorol. Soc.* **2018**, *144*, 270–281. [CrossRef]
11. Zoccatelli, D.; Borga, M.; Zanon, F.; Antonescu, B.; Stancalie, G. Which rainfall spatial information for flash flood response modelling? A numerical investigation based on data from the Carpathian range, Romania. *J. Hydrol.* **2010**, *394*, 148–161. [CrossRef]
12. Kidd, C.; Levizzani, V. Status of satellite precipitation retrievals. *Hydrol. Earth Syst. Sci.* **2011**, *15*, 1109–1116. [CrossRef]
13. Wang, H.; Wang, L.; He, J.; Ge, F.; Chen, Q.; Tang, S.; Yao, S. Can the GPM IMERG Hourly Products Replicate the Variation in Precipitation During the Wet Season Over the Sichuan Basin, China? *Earth Space Sci.* **2020**, *7*, e2020EA001090. [CrossRef]
14. Mishra, V.; Shah, R.D. Development of an Experimental Near-Real-Time Drought Monitor for India. *J. Hydrometeorol.* **2015**, *16*, 327–345. [CrossRef]
15. Mekonnen, K.; Melesse, A.M.; Woldesenbet, T.A. Spatial evaluation of satellite-retrieved extreme rainfall rates in the Upper Awash River Basin, Ethiopia. *Atmos. Res.* **2021**, *249*, 105297. [CrossRef]
16. Solakian, J.; Maggioni, V.; Godrej, A.N. On the Performance of Satellite-Based Precipitation Products in Simulating Streamflow and Water Quality During Hydrometeorological Extremes. *Front. Environ. Sci.* **2020**, *8*, 585451. [CrossRef]
17. Soo, E.Z.X.; Wan Jaafar, W.Z.; Lai, S.H.; Othman, F.; Elshafie, A.; Islam, T.; Srivastava, P.; Othman Hadi, H.S. Precision of raw and bias-adjusted satellite precipitation estimations (TRMM, IMERG, CMORPH, and PERSIANN) over extreme flood events: Case study in Langat river basin, Malaysia. *J. Water Clim. Chang.* **2020**, *11*, 322–342. [CrossRef]
18. Zhu, B.; Huang, Y.; Zhang, Z.; Kong, R.; Tian, J.; Zhou, Y.; Chen, S.; Duan, Z. Evaluation of TMPA Satellite Precipitation in Driving VIC Hydrological Model over the Upper Yangtze River Basin. *Water* **2020**, *12*, 3230. [CrossRef]
19. Zema, D.A.; Labate, A.; Martino, D.; Zimbone, S.M. Comparing Different Infiltration Methods of the HEC-HMS Model: The Case Study of the Mésima Torrent (Southern Italy). *Land Degrad. Dev.* **2016**, *28*, 294–308. [CrossRef]
20. Zhou, L.; Rasmy, M.; Takeuchi, K.; Koike, T.; Selvarajah, H.; Ao, T. Adequacy of Near Real-Time Satellite Precipitation Products in Driving Flood Discharge Simulation in the Fuji River Basin, Japan. *Appl. Sci.* **2021**, *11*, 1087. [CrossRef]
21. Habib, E.; Haile, A.; Sazib, N.; Zhang, Y.; Rientjes, T. Effect of Bias Correction of Satellite-Rainfall Estimates on Runoff Simulations at the Source of the Upper Blue Nile. *Remote Sens.* **2014**, *6*, 6688–6708. [CrossRef]
22. Tian, Y.; Peters-Lidard, C.D.; Eylander, J.B. Real-Time Bias Reduction for Satellite-Based Precipitation Estimates. *J. Hydrometeorol.* **2010**, *11*, 1275–1285. [CrossRef]
23. Borga, M.; Tonelli, F.; Moore, R.J.; Andrieu, H. Long-term assessment of bias adjustment in radar rainfall estimation. *Water Resour. Res.* **2002**, *38*, 8-1–8-10. [CrossRef]
24. Ren, P.; Li, J.; Feng, P.; Guo, Y.; Ma, Q. Evaluation of Multiple Satellite Precipitation Products and Their Use in Hydrological Modelling over the Luanhe River Basin, China. *Water* **2018**, *10*, 677. [CrossRef]
25. Zhang, L.; Li, X.; Zheng, D.; Zhang, K.; Ma, Q.; Zhao, Y.; Ge, Y. Merging multiple satellite-based precipitation products and gauge observations using a novel double machine learning approach. *J. Hydrol.* **2021**, *594*, 125969. [CrossRef]
26. Shen, C. A Transdisciplinary Review of Deep Learning Research and Its Relevance for Water Resources Scientists. *Water Resour. Res.* **2018**, *54*, 8558–8593. [CrossRef]
27. Kumar, D.; Singh, A.; Samui, P.; Jha, R.K. Forecasting monthly precipitation using sequential modelling. *Hydrol. Sci. J.* **2019**, *64*, 690–700. [CrossRef]
28. Oshri, B.; Hu, A.; Adelson, P.; Chen, X.; Dupas, P.; Weinstein, J.; Burke, M.; Lobell, D.; Ermon, S. Infrastructure Quality Assessment in Africa using Satellite Imagery and Deep Learning. In Proceedings of the 24th ACM SIGKDD International Conference on Knowledge Discovery & Data Mining, London, UK, 19–23 August 2018; pp. 616–625.
29. Tao, Y.M.; Gao, X.G.; Hsu, K.L.; Sorooshian, S.; Ihler, A. A Deep Neural Network Modeling Framework to Reduce Bias in Satellite Precipitation Products. *J. Hydrometeorol.* **2016**, *17*, 931–945. [CrossRef]
30. Wu, H.; Yang, Q.; Liu, J.; Wang, G. A spatiotemporal deep fusion model for merging satellite and gauge precipitation in China. *J. Hydrol.* **2020**, *584*, 124664. [CrossRef]
31. Wang, X.; Li, B.; Chen, Y.; Guo, H.; Wang, Y.; Lian, L. Applicability Evaluation of Multisource Satellite Precipitation Data for Hydrological Research in Arid Mountainous Areas. *Remote Sens.* **2020**, *12*, 2886. [CrossRef]
32. Derin, Y.; Anagnostou, E.; Berne, A.; Borga, M.; Boudevillain, B.; Buytaert, W.; Chang, C.-H.; Chen, H.; Delrieu, G.; Hsu, Y.; et al. Evaluation of GPM-era Global Satellite Precipitation Products over Multiple Complex Terrain Regions. *Remote Sens.* **2019**, *11*, 2936. [CrossRef]
33. Freitas, E.d.S.; Coelho, V.H.R.; Xuan, Y.; Melo, D.d.C.D.; Gadelha, A.N.; Santos, E.A.; Galvão, C.d.O.; Ramos Filho, G.M.; Barbosa, L.R.; Huffman, G.J.; et al. The performance of the IMERG satellite-based product in identifying sub-daily rainfall events and their properties. *J. Hydrol.* **2020**, *589*, 125128. [CrossRef]
34. Wang, S.; Liu, J.; Wang, J.; Qiao, X.; Zhang, J. Evaluation of GPM IMERG V05B and TRMM 3B42V7 Precipitation Products over High Mountainous Tributaries in Lhasa with Dense Rain Gauges. *Remote Sens.* **2019**, *11*, 2080. [CrossRef]
35. Bhatti, H.A.; Rientjes, T.; Haile, A.T.; Habib, E.; Verhoef, W. Evaluation of Bias Correction Method for Satellite-Based Rainfall Data. *Sensors* **2016**, *16*, 884. [CrossRef] [PubMed]
36. Anagnostou, E.N.; Nikolopoulos, E.I.; Ehsan Bhuiyan, M.A. Machine Learning–Based Blending of Satellite and Reanalysis Precipitation Datasets: A Multiregional Tropical Complex Terrain Evaluation. *J. Hydrometeorol.* **2019**, *20*, 2147–2161. [CrossRef]

37. Peng, F.; Zhao, S.; Chen, C.; Cong, D.; Wang, Y.; Ouyang, H. Evaluation and comparison of the precipitation detection ability of multiple satellite products in a typical agriculture area of China. *Atmos. Res.* **2020**, *236*, 104814. [CrossRef]
38. Bhuiyan, M.A.E.; Yang, F.; Biswas, N.K.; Rahat, S.H.; Neelam, T.J. Machine Learning-Based Error Modeling to Improve GPM IMERG Precipitation Product over the Brahmaputra River Basin. *Forecasting* **2020**, *2*, 14. [CrossRef]
39. Ding, L.; Ma, L.; Li, L.; Liu, C.; Li, N.; Yang, Z.; Yao, Y.; Lu, H. A Survey of Remote Sensing and Geographic Information System Applications for Flash Floods. *Remote Sens.* **2021**, *13*, 1818. [CrossRef]
40. He, J.; Zhang, K.; Liu, X.; Liu, G.; Zhao, X.; Xie, Z.; Lu, H. Vegetation restoration monitoring in Yingxiu landslide area after the 2008 Wenchuan earthquake. *Earthq. Res. China* **2020**, *34*, 157–166. [CrossRef]
41. Lu, H.; Ma, L.; Fu, X.; Liu, C.; Wang, Z.; Tang, M.; Li, N. Landslides Information Extraction Using Object-Oriented Image Analysis Paradigm Based on Deep Learning and Transfer Learning. *Remote Sens.* **2020**, *12*, 752. [CrossRef]
42. Lo Conti, F.; Hsu, K.-L.; Noto, L.V.; Sorooshian, S. Evaluation and comparison of satellite precipitation estimates with reference to a local area in the Mediterranean Sea. *Atmos. Res.* **2014**, *138*, 189–204. [CrossRef]
43. Huffman, G.J.; Stocker, E.F.; Bolvin, D.T.; Kelkin, E.J.; Tan, J. *GPM IMERG Late Precipitation L3 1 Day 0.1 Degree×0.1 Degree V06*; Andrey, S., Greenbelt, M.D., Eds.; Goddard Earth Sciences Data and Information Services Center (GES DISC): Washington, DC, USA, 2019. Available online: https://disc.gsfc.nasa.gov/datasets/GPM_3IMERGDF_06/summary (accessed on 1 May 2020).
44. FAO/IIASA/ISRIC/ISS-CAS/JRC. *Harmonized World Soil Database (Version 1.1)*; FAO: Rome, Italy; IIASA: Laxenburg, Austria, 2009; Available online: http://www.fao.org/3/a-aq361e.pdf (accessed on 1 May 2020).
45. De Villiers, J.; Barnard, E. Backpropagation neural nets with one and two hidden layers. *IEEE Trans. Neural Netw.* **1993**, *4*, 136–141. [CrossRef]
46. Hornik, K.; Stinchcombe, M.; White, H. Multilayer Feedforward Networks Are Universal Approximators. *Neural Netw.* **1989**, *2*, 359–366. [CrossRef]
47. Cheng, X.; Ma, X.; Wang, W.; Xiao, Y.; Wang, Q.; Liu, X. Application of HEC-HMS Parameter Regionalization in Small Watershed of Hilly Area. *Water Resour. Manag.* **2021**, *35*, 1961–1976. [CrossRef]
48. El Hassan, A.A.; Sharif, H.O.; Jackson, T.; Chintalapudi, S. Performance of a conceptual and physically based model in simulating the response of a semi-urbanized watershed in San Antonio, Texas. *Hydrol. Process.* **2013**, *27*, 3394–3408. [CrossRef]
49. Bai, Y.; Zhang, Z.; Zhao, W. Assessing the Impact of Climate Change on Flood Events Using HEC-HMS and CMIP5. *Water Air Soil Pollut.* **2019**, *230*, 119. [CrossRef]
50. Mohammadi Hashemi, M.; Saghafian, B.; Zakeri Niri, M.; Najarchi, M. Applicability of Rainfall–Runoff Models in Two Simplified Watersheds. *Iran. J. Sci. Technol. Trans. Civ. Eng.* **2021**. [CrossRef]
51. Hussain, F.; Wu, R.-S.; Yu, K.-C. Application of Physically Based Semi-Distributed Hec-Hms Model for Flow Simulation in Tributary Catchments of Kaohsiung Area Taiwan. *J. Mar. Sci. Technol.* **2021**, *29*, 4. [CrossRef]
52. Belayneh, A.; Sintayehu, G.; Gedam, K.; Muluken, T. Evaluation of satellite precipitation products using HEC-HMS model. *Model. Earth Syst. Environ.* **2020**, *6*, 2015–2032. [CrossRef]
53. Kazezyılmaz-Alhan, C.M.; Yalçın, İ.; Javanshour, K.; Aytekin, M.; Gülbaz, S. A hydrological model for Ayamama watershed in Istanbul, Turkey, using HEC-HMS. *Water Pract. Technol.* **2021**, *16*, 154–161. [CrossRef]
54. Gilewski, P.; Nawalany, M. Inter-Comparison of Rain-Gauge, Radar, and Satellite (IMERG GPM) Precipitation Estimates Performance for Rainfall-Runoff Modeling in a Mountainous Catchment in Poland. *Water* **2018**, *10*, 1665. [CrossRef]
55. Baez-Villanueva, O.M.; Zambrano-Bigiarini, M.; Beck, H.E.; McNamara, I.; Ribbe, L.; Nauditt, A.; Birkel, C.; Verbist, K.; Giraldo-Osorio, J.D.; Xuan Thinh, N. RF-MEP: A novel Random Forest method for merging gridded precipitation products and ground-based measurements. *Remote Sens. Environ.* **2020**, *239*, 111606. [CrossRef]
56. Mei, Y.; Nikolopoulos, E.I.; Anagnostou, E.N.; Borga, M. Evaluating Satellite Precipitation Error Propagation in Runoff Simulations of Mountainous Basins. *J. Hydrometeorol.* **2016**, *17*, 1407–1423. [CrossRef]